Effect of carbon on elastic properties and microstructure of maraging steel : First-principles and phase-field study

Vsevolod Razumovskiy[a,*], Hemantha Kumar Yeddu[b], Jürgen Spitaler[a]

[a]*Materials Center Leoben Forschung GmbH (MCL),Roseggerstraße 12, A-8700 Leoben, Austria.*

[b]*School of Engineering, Newcastle University, Newcastle upon Tyne, NE1 7RU, United Kingdom.*

Abstract

The effect of the carbon concentration on the elastic properties and martensitic microstructure of Marval X12 steel is studied using first principles calculations and phase-field simulations. The density functional theory (DFT) results predict almost no changes of the elastic moduli with an increase of C content. However, there is a sizeable change of the elastic constants due to cubic to tetragonal martensitic transformation. The elastic constants are used as input data for the 3D elastoplastic phase-field model to study the martensitic microstructure evolution in Marval X12 steel. The results, showing that lath martensite is formed in this steel, are in agreement with experiments. With increasing carbon concentration, we observe formation of mixed morphology predominantly composed of martensite laths and some martensite plates. Our results also suggest that different combinations of martensite variants are formed with increasing carbon content.

Keywords: Elastic constants, ab initio calculations, phase-field model, martensitic transformation, microstructure, steels

*Corresponding Author. E-mail: razvsevol@yahoo.com

1. Introduction

Maraging steels have been used in military and aerospace industries due to their high strength and toughness, good damage tolerance, high strength to weight ratio [1–3]. The good mechanical properties of maraging steels are due to the microstructure that consists of lath martensite formed during quenching, intermetallic precipitates and reverted austenite that form during aging [3]. The lath martensitic microstructure and the intermetallic precipitates improve the hardness by obstructing the dislocation motion. The ductility and toughness are improved by reverted austenite that forms due to the reverse phase transformation of martensite to austenite during aging [4, 5].

Experiments have shown that a small fraction of austenite, either retained or reverted, can be present in PH13-8 Mo maraging steels [6, 7]. Both types of austenite affect the toughness of maraging steels [8]. It has been reported that austenite can transform to martensite under the influence of elastic stress and can cause transformation induced plasticity (TRIP) effect [9–11]. Under the influence of stresses greater than the yield stress, austenite can transform to strain-induced martensite [12]. Therefore, it is essential to predict the formation of martensite and retained austenite in maraging steels.

Marval X12 steel is a maraging steel with a composition of Fe - 12 Cr - 9 Ni - 2 Mo - 0.9 Al - 0.3 Ti - 0.02 C, expressed in weight %. The effects of alloying elements on martensite formation and mechanical properties of maraging steels have been studied previously [13, 14]. Titanium does not show a significant effect on martensite start (M_s) and finish (M_f) temperature, whereas

chromium promotes stabilization of austenite and shifts the M_s temperature [13]. Carbon content in maraging steels is limited to 0.03 wt.% in order to obtain lath martensite and because of the ability of carbon to form grain boundary carbides with titanium that can cause embrittlement [14]. The carbon content can be increased in maraging steels that do not contain titanium and hence grain boundary carbides can be avoided [14]. Increased carbon content leads to increased amount of residual austenite in maraging steels [14]. An increase in the carbon content affects the morphology of martensite. A low carbon steel can give rise to lath martensite, whereas a high carbon steel can give rise to plate martensite [15, 16]. The mechanical properties of these two morphologies can be different [16] and therefore it is practically important to know whether the morphology of Marval X12-type of maraging steels can be affected by changing the C content.

The phase field method [17, 18] represents the theoretical approach of choice to address this problem. It has already been successfully applied to study martensitic transformations [19–26] as well as the reversion of martensite to austenite [27] in numerous research papers. In the present work, a 3D phase-field model coupled with continuum plasticity [19], including strain hardening [28], is used to study the martensitic microstructure evolution in Marval X12 steel. The elastic constants as well as crystal structure changes [29] of the steel with variations in C-content are investigated by means of first principles calculations. We use the results of these first principles calculations along with the thermodynamic data from Thermo-Calc [30] to predict possible martensite morphology in Marval X12-type of steels with different carbon contents.

2. Methodology

2.1. Elasic constants calculations

Elastic constants and elastic moduli in this work have been calculated following the methodology described in [23, 31, 32]. A uniform lattice distortion in the elastic property calculations has been imposed on the lattice by transforming the set of primitive vectors, a_i, to a set of new vectors, a_i':

$$\begin{pmatrix} a_1' \\ a_2' \\ a_3' \end{pmatrix} = (\boldsymbol{I} + \varepsilon) \cdot \begin{pmatrix} a_1 \\ a_2 \\ a_3 \end{pmatrix}, \tag{1}$$

where $\boldsymbol{I}$ is the 3×3 identity matrix and ε is a symmetric strain tensor:

$$\varepsilon = \begin{pmatrix} e_1 & e_6/2 & e_5/2 \\ e_6/2 & e_2 & e_4/2 \\ e_5/2 & e_4/2 & e_3 \end{pmatrix}. \tag{2}$$

The total energy change (ΔE) at zero pressure/zero volume change reads as:

$$\Delta E = V \sum_{i=1}^{6} \sum_{j=1}^{6} C_{ij} e_i e_j / 2 + O[e_i^3], \tag{3}$$

where V is the equilibrium volume, C_{ij} are the elastic constants, e_i and e_j are the components of the strain tensor and the $O[e_i^3]$ term indicates that cubic and higher powers of e_i are neglected in the expansion.

There are 21 independent elastic constants, C_{ij}, but symmetry of the cubic lattice reduces this number to only 3 independent constants (C_{11}, C_{12},

and C_{44}) for cubic lattices. A uniform isotropic straining (compression or expansion) of the lattice gives one the access to the bulk modulus, B, which is a linear combination of two elastic constants,

$$B = (C_{11} + 2C_{12})/3 \tag{4}$$

and can be directly obtained from the equation of state (EQOS) DFT calculations . The calculation of B reduces the number of necessary C_{ij} calculations to two volume-conserving strains shown in terms of related lattice distortions x in Table 1. In the case of the tetragonal lattice, the number of elastic constants increases to six (see Table 1) and the relation between them and the bulk modulus reads as follows:

$$B = \left((C_{11} + C_{12})\, C_{33} - 2C_{13}^2\right) / \left(C_{11} + C_{12} + 2C_{33} - 4C_{13}\right). \tag{5}$$

The value of distortion x has been varied from zero (for the equilibrium state) to ± 0.05 with a step size of 0.01 for the cubic case and from zero to ± 0.03 with a step size of 0.01 for the tetragonal case, in accordance with Mehl *et. al.*'s prescription [31].

Polycrystalline Young modulus E and shear moduli G are evaluated using the obtained single crystal elastic constants as follows. There is no exact expression for the polycrystalline-averaged shear modulus in terms of the C_{ij}, but one can evaluate approximate "averages" of the lower and upper bounds.

In the case of cubic symmetry, the upper bound due to Voight [33] is calculated as:

$$G_V = \frac{C_{11} - C_{12} + 3C_{44}}{5}, \tag{6}$$

Table 1: Strain and energy changes for the cubic and tetragonal phases after Ref. [31]. Non-listed e_i are set to 0.

Strain	Parameters	$\Delta E/V$
Cubic lattice		
1	$e_1 = -e_2 = x$	
	$e_3 = x^2/(1-x^2)$	$(C_{11}-C_{12})x^2 + O[x^4]$
2	$e_3 = x^2/(4-x^2)$	
	$e_6 = x$	$(1/2)C_{44}x^2 + O[x^4]$
Tetragonal lattice		
1	$e_1 = e_2 = x$	$(C_{11}+C_{12})x^2 + O[x^3]$
2	$e_1 = e_2 = x$	
	$e_3 = -x(2+x)/(1+x)^2$	$(C_{11}+C_{12}+2C_{33}-4C_{13})x^2 + O[x^3]$
3	$e_3 = x$	$(C_{33}x^2/2) + O[x^3]$
4	$e_1 = ((1+x)/(1-x))^{0.5} - 1$	
	$e_2 = ((1-x)/(1+x))^{0.5} - 1$	$(C_{11}-C_{12})x^2 + O[x^4]$
5	$e_4 = e_5 = x, e_3 = x^2/4$	$C_{44}x^2 + O[x^4]$
6	$e_6 = x$	
	$e_1 = e_2 = (1+x^2/4)^{0.5} - 1$	$C_{66}x^2/2 + O[x^4]$

and the lower bound due to Reuss [34] reads:

$$G_R = \frac{5(C_{11}-C_{12})C_{44}}{4C_{44}+3(C_{11}-C_{12})}. \tag{7}$$

In the case of tetragonal symmetry, these expressions read as follows:

$$G_V = (2C_{11}+C_{33}-C_{12}-2C_{13}+6C_{44}+3C_{66})/15, \tag{8}$$

and the lower bound due to Reuss [34] reads:

$$G_R = 15C(C_{11} - C_{12})C_{44}C_{66}/(2(C_{11} - C_{12})(2(C_{11} + C_{12}) + 4C_{13} + C_{33})C_{44}C_{66} + 3C(2C_{44}C_{66} + (C_{11} - C_{12})(C_{44} + 2C_{66}))), \quad (9)$$

where

$$C = C_{33}(C_{11} + C_{12}) - 2C_{13}^2. \quad (10)$$

According to Hill [35], the arithmetic average of the Voight and Reuss values can be used as an estimate of the average shear modulus:

$$G = \frac{G_V + G_R}{2}. \quad (11)$$

Using this estimate of G, we evaluate the polycrystalline-averaged Young's modulus as

$$E = \frac{9BG}{3B + G}. \quad (12)$$

2.2. Computational details

Spin polarized density functional theory (DFT) calculations of the total energy in this work have been performed using the projector-augmented-wave (PAW) [36, 37] method as implemented in the Vienna ab initio simulation package (VASP) [38, 39]. We have used the generalized gradient approximation (GGA) to the exchange-correlation potential[40, 41]. The VASP-PAW calculations have been performed using a plane-wave cutoff energy of 400 eV. The convergence criteria have been chosen to be 10^{-7} eV for the total energy and 9×10^{-3} eV/Å for the forces. Ionic relaxations were included in all calculations. The integration over the Brillouin zone has been done using the

$6 \times 6 \times 6$ Monkhorst-Pack mesh [42] for the largest $4 \times 4 \times 4 \times$[conventional bcc cell] supercell (SC) that has been changed proportionally to the cell size of other supercells used in the calculations using smaller SCs [see Sec. 2.3] to keep a constant k-point density.

The exact muffin-tin orbital (EMTO) method [43, 44] implemented in the Green's function formalism and combined with the full charge density (FCD) technique [45] has been used in the coherent potential approximation (CPA) [46] calculations of disordered alloys. The paramagnetic state of these alloys has been modeled by the disordered local moment (DLM) [47, 48] model. All self-consistent DLM-CPA calculations have been performed using the orbital momentum cut-off of $l_{\max} = 3$ for partial waves. The integration over the Brillouin zone has been performed using $37 \times 37 \times 37$ Monkhorst-Pack grids of k-points [42] for both fcc and bcc structures. The core states have been recalculated at each self-consistent iteration. The screening constants for the screened Coulomb interactions have been obtained by the EMTO-LSGF (locally self-consistent Green function method) method [49].

The equation of state and its parameters have been obtained using the Birch-Murnaghan fit [50]. All structures have been rendered using the VESTA programme package [51].

2.3. Elastic constants of random alloys

Elastic constants of random alloys in EMTO-CPA calculations have been calculated as described in Sec. 2.1 using 1-atom primitive fcc and bcc cells. Elastic constants of a random $Fe_{78.125}Cr_{12.5}Ni_{9.375}$ alloy in VASP-PAW calculations have been calculated using a $4 \times 4 \times 4 \times$ [conventional bcc cell] supercell (SC) of 128-sites. Hereby and in what follows, all concentrations

are given in atomic percent.

We have used the following supercell configurations to model Fe-Cr-Ni-C random alloys in the VASP-PAW calculations: i) $4\times4\times4$ $\times$[conventional bcc cell] (128-site , $Fe_{78.125}Cr_{12.50}Ni_{9.375}$ and 128-site + 1C, $Fe_{77.52}Cr_{12.40}Ni_{9.30}C_{0.78}$); ii) $3 \times 3 \times 3$ (54-site + 1C, $Fe_{76.36}Cr_{12.72}Ni_{9.10}C_{1.82}$); iii) $2 \times 2 \times 2$ (16-site + 1C,$Fe_{76.48}Cr_{11.76}Ni_{5.88}C_{5.88}$). Fe, Cr and Ni atoms have been disrtibuted on the metal-atom sublattice in a way that their pair correlation functions (Warren-Cowley short range order parameters) are as close as possible to zero (referring to a completely disordered distribution of atoms) at the first four coordination shells (see Supplimentary material for details). The carbon atom has always been placed in such atomic environment that represents as closely as possible the chemical composition of the random alloy at the first coordination sphere as it is shown in Figure 1. Exact values of the short range order parameters in the optimized supercells for all alloys are provided as Supplimentary material.

Prepared supercell structures have been fully relaxed including volume, shape and atomic positions relaxations. The presence of atomic disorder at atomic level in the created SC introduces minor changes of the crystal symmetry leading to slightly orthorhombic rather than cubic (in the case of ferrite in C-free steels) or tetragonal (in the case of martensite) symmetries observed in experiment [52]. We have tried to remove this artefact of the SC construction by averaging out the deviating lattice constants a, b and c after the full relaxation (a_{rel}, b_{rel} and c_{rel}) and using the averaged values along with the the experimentally observed crystallographic geometry in all elastic constants calculations. After fixing the cell shape to a=b=c=$(a_{rel} + b_{rel} + c_{rel})$ /3 for

the case with no C and to $a{=}a_{rel} \neq b{=}c{=}(b_{rel}+c_{rel})/2$ for the case of alloys with C, the atomic positions and the cell volume have been additionally relaxed prior to the elastic constants calculations.

2.4. Phase-field model

The martensitic microstructure evolution is governed by the phase-field equation [19, 20]:

$$\frac{\partial \eta_p}{\partial t} = -L \sum_{p=1}^{p=3} \left(\frac{\partial G_v^{chem}}{\partial \eta_p} + \frac{\partial G_v^{el}}{\partial \eta_p} - \frac{1}{2}\beta \frac{\partial \eta_p}{\partial r_i}\frac{\partial \eta_p}{\partial r_j} \right) \tag{13}$$

where η_p is the phase field variable that tracks the evolution of martensite units, $\mathbf{r(x,y,z)}$ is the position vector expressed in Cartesian coordinates, L governs the mobility of the phase interface, G_v^{chem} is the chemical part of the Gibbs energy density and G_v^{el} is the strain energy density. The last term in Eq. (13) is the gradient energy term (G_v^{grad}) and β is the gradient energy coefficient expressed in terms of the interfacial energy (γ), molar volume (V_m) and the Gibbs energy barrier as: $\beta = \frac{9\gamma^2 V_m}{16\Delta G^*}$.

Martensite variants (laths) can form in 24 different crystallographic orientations. Based on the axis of compression of the variants, they can be grouped into three basic variants known as Bain variants [53, 54]. In this work formation of the three Bain variants is modelled by considering three phase-field variables η_1, η_2 and η_3. G_v^{chem} is expressed as a Landau-type polynomial in terms of the three phase-field variables [19, 20]:

$$\begin{aligned} G_v^{chem}(\eta_1,\eta_2,\eta_3) = \frac{1}{V_m}\Bigg[& \frac{1}{2}A\left(\eta_1^2+\eta_2^2+\eta_3^2\right) - \frac{1}{3}B\left(\eta_1^3+\eta_2^3+\eta_3^3\right) \\ & + \frac{1}{4}C\left(\eta_1^2+\eta_2^2+\eta_3^2\right)^2 \Bigg] \end{aligned} \tag{14}$$

where the coefficients A, B, C are expressed in terms of Gibbs energy barrier (ΔG^*) and the driving force (ΔG_m) as: $A = 32\Delta G^*$, $B = (3A - 12\Delta G_m)$, $C = (2A - 12\Delta G_m)$ and $\Delta G^* = \frac{V_m \beta}{2\delta^2}$ [19]. δ is the physical interface thickness.

G_v^{el} can be expressed as [19, 20, 22]:

$$G_v^{el} = \int_{\epsilon_{ij}^0(\mathbf{r})}^{\epsilon_{ij}(\mathbf{r})} \sigma_{ij}(\mathbf{r}) d\epsilon_{ij}(\mathbf{r}) = \int_{\epsilon_{ij}^0(\mathbf{r})}^{\epsilon_{ij}(\mathbf{r})} c_{ijkl} \left(\epsilon_{kl}(\mathbf{r}) - \epsilon_{kl}^0(\mathbf{r}) - \epsilon_{kl}^{pl}(\mathbf{r}) \right) d\epsilon_{ij}(\mathbf{r}) \tag{15}$$

where $\sigma_{ij}(\mathbf{r})$ is the stress, c_{ijkl} is the tensor of elastic constants, $\epsilon_{ij}(\mathbf{r})$ is the total strain, $\epsilon_{ij}^0(\mathbf{r})$ is the stress-free transformation strain and $\epsilon_{kl}^{pl}(\mathbf{r})$ is the plastic strain. The total strain $\epsilon_{ij}(\mathbf{r})$ is calculated by solving the mechanical equilibrium equation $\frac{\partial \sigma_{ij}(\mathbf{r})}{\partial r_j} = 0$, expressed as:

$$c_{ijkl} \left(\frac{\partial \epsilon_{kl}(\mathbf{r})}{\partial r_j} - \frac{\partial \epsilon_{kl}^0(\mathbf{r})}{\partial r_j} - \frac{\partial \epsilon_{kl}^{pl}(\mathbf{r})}{\partial r_j} \right) = 0 \tag{16}$$

Small strain theory is assumed in the present work and therefore $\epsilon_{ij}(\mathbf{r}) = \frac{1}{2} \left(\frac{\partial u_i(\mathbf{r})}{\partial r_j} + \frac{\partial u_j(\mathbf{r})}{\partial r_i} \right)$, where $\mathbf{u(r)}$ is the local displacement vector.

$\epsilon_{ij}^0(\mathbf{r})$ is given by:

$$\epsilon_{ij}^0(\mathbf{r}) = \sum_{p=1}^{p=3} \eta_p(\mathbf{r}) \epsilon_{ij}^{00}(p) \tag{17}$$

where $\epsilon_{ij}^{00}(p)$ are the Bain strain tensors that govern the three phase-field variables (η_1, η_2 and η_3) and are given by:

$$\epsilon_{ij}^{00}(1) = \begin{bmatrix} \epsilon_3 & 0 & 0 \\ 0 & \epsilon_1 & 0 \\ 0 & 0 & \epsilon_1 \end{bmatrix}, \epsilon_{ij}^{00}(2) = \begin{bmatrix} \epsilon_1 & 0 & 0 \\ 0 & \epsilon_3 & 0 \\ 0 & 0 & \epsilon_1 \end{bmatrix}, \epsilon_{ij}^{00}(3) = \begin{bmatrix} \epsilon_1 & 0 & 0 \\ 0 & \epsilon_1 & 0 \\ 0 & 0 & \epsilon_3 \end{bmatrix} \tag{18}$$

where ϵ_3 is a compressive transformation strain, ϵ_1 is a tensile transformation strain and are defined based on the lattice constants of austenite (a_{FCC}) and

martensite (a_{BCC}, c_{BCC}) as: [19]. Thus the martensite (Bain) variants 1, 2 and 3 are governed by $\epsilon_{ij}^{00}(1)$, $\epsilon_{ij}^{00}(2)$ and $\epsilon_{ij}^{00}(3)$, respectively.

The plastic strain ($\epsilon_{kl}^{pl}(\mathbf{r})$) is generated when the internal stress ($\sigma_{ij}(\mathbf{r})$) exceeds the yield limit and the material undergoes plastic deformation. In the present work, the von Mises yield criterion is used. The evolution of plastic strain $\epsilon_{ij}^{pl}(\mathbf{r})$ is governed by [19, 22]:

$$\frac{\partial \epsilon_{ij}^{pl}(\mathbf{r})}{\partial t} = -k_{ijkl} \frac{\delta G_v^{shear}}{\delta \epsilon_{kl}^{pl}(\mathbf{r})} \tag{19}$$

where G_v^{shear} is the shear energy density expressed in terms of deviatoric strain components [19], k_{ijkl} ($= kc_{ijkl}^{-1}$) is the plastic kinetic coefficient and c_{ijkl}^{-1} is the compliance tensor. k is a parameter, which controls the rate at which stresses are relaxed by means of plastic deformation and is called plastic relaxation rate [19]. Linear isotropic strain hardening is considered by using the expression $\sigma_y = \sigma_y^0 + H\epsilon^{pl}(\mathbf{r})$ [55], where σ_y is the yield stress of the material that depends on plastic strain, σ_y^0 is initial yield stress, H is hardening modulus and $\epsilon^{pl}(\mathbf{r})$ is equivalent plastic strain.

The elastic modulii of FCC, BCC and BCT phases are acquired from *ab initio* calculations, as explained in Section 2.1. The anisotropic elastic properties of different phases are considered by using $c_{ijkl} = c_{ijkl}^{FCC}(1 - \eta_p) + c_{ijkl}^{BCCorBCT}\eta_p$. Hence the elastic modulii c_{ijkl}^{FCC} or $c_{ijkl}^{BCCorBCT}$ are considered when $\eta_p = 0$ or $\eta_p = 1$, respectively and in the interface a weighted c_{ijkl} that depends on the weight yielded by the phase-field variable is considered.

2.4.1. Phase-field simulation data

Table-2 shows the data used to study Marval X12 steel (Fe-12.8 at %Cr-8.5 at %Ni) as well as the steels with increased carbon content. The data

is calculated using the CALPHAD method and *ab initio* method as well as acquired from experiments. Table-3 shows the lattice constants used in the phase-field simulations. The lattice constants of the Marval X12 steel are acquired from experimental data [56]. The variation of lattice constants with increasing carbon content of Marval X12 steels is estimated by assuming that the trend is similar to that of Fe-C alloys [29].

Table 2: Simulation data.

M_s temperature of Marval X12 steel: 421 K [57]
Thermodynamic coefficients: A = 1188 J/mol, B = 3564 J/mol,
C = 2376 J/mol [19]
Gradient coefficient (β) = 0.1061 x 10^{-10} J/m [19]
Driving forces (J/mol) at T= 421 K are: –3612, –3000, –2550, –2327 and
–1995 for the alloys shown in Table-3, respectively [30]
Molar volume (V_m) = 7 x 10^{-6} m^3/mol
Gibbs energy barrier (ΔG^*) = 37.135 J/mol
Interfacial energy (γ) = 0.01 J/m^2 [20]
Lattice constants: See Table-3
Elastic constants of the fcc phase of different alloys: See Table- 5
Elastic constants of the bcc phase of different alloys: See Fig. 3
Initial yield stresses: σ_y^0 (fcc) = 500 MPa [58], σ_y^0 (bct) = 800 MPa [59].
H = 738 MPa [60].
Plastic relaxation rate (k) = 0.2 $GPa^{-1}s^{-1}$
Interfacial kinetic coefficient (L) = 1 $m^3J^{-1}s^{-1}$

Table 3: Alloy compositions and lattice constants.

	fcc	*bcc* or *bct*		
Alloy composition (at. %)	a (Å)	a (Å)	c (Å)	c/a
Fe-12.8Cr-8.5Ni [56]	3.6024	2.881	2.881	1
Fe-12.8Cr-8.5Ni-0.78C	3.6106	2.8784	2.9014	1.0080
Fe-12.8Cr-8.5Ni-1.8C	3.6216	2.8752	2.929	1.0187
Fe-12.8Cr-8.5Ni-4.5C	3.6504	2.8681	3.001	1.0463
Fe-12.8Cr-8.5Ni-5.75C	3.6648	2.8652	3.037	1.0599

Simulations are performed on austenite single crystal of 1 μm grain size by using FemLego software [61]. A pre-existing spherical martensite (η_1) embryo of 0.1 μm is considered in the center of the grain. All the phase-field simulations are performed at the experimental M_s temperature of 421 K. Dirichlet (clamped) boundary conditions are considered. The plastic relaxation rate (k) is a model parameter and is chosen to be independent of alloy composition. The values of physical interface width (δ) and Gradient coefficient (β) considered in the simulations ensure that the transformation is not completely barrier-less and also that the energy barrier is not too large such that the transformation is inhibited.

The grid size considered is 50 x 50 x 50 to simulate a three dimensional 1 μm grain. Hence the width of each grid element is 20 nm. In the simulations three grid elements were considered as the interface width. Therefore, for better numerical accuracy, the actual interface width considered in the simulations is 60 nm compared to the physical interface thickness of 1 nm used to calculate the Gibbs energy barrier. In one of the authors' recent work, an interface width of 30 nm is considered to simulate martensite formation in

a two dimensional (2D) grain of 1 micron [25]. On comparing the present results with the previous results, we do not see any significant dependence of the microstructure on interface width considered in the simulations.

As the experimental data related to the mobility of the martensitic interface is ambiguous, the interface mobility (L) in Eq. (13) is considered to be unity. Due to the dependence of time (t) on the ambiguous parameter L_{pq}, the time scale is expressed in terms of dimensionless time t*, where $t^* = LRTt/V_m$.

3. Results and discussion

3.1. DFT results

3.1.1. Phase stability at 0 K

As a first step in our study we have evaluated stability of the fcc (austenitic) and bcc (ferritic) phases of Marval X12 carbon free steel $Fe_{76}Ni_{8.3}Cr_{12.6}Al_{1.4}$ $Si_{0.1}Ti_{0.4}Mn_{0.03}Mo_{1.14}$ using EMTO DFT calculations at 0K. The results shown in Figure 2a demonstrate that both bcc and fcc phases prefer the ferromagnetic (FM) over the paramagnetic (PM) state (represented in our calculation via the DLM model) at 0K. The most stable phase at 0K has been found to be FM bcc. As the cell volume decreases, the fcc FM phase undergoes a high-spin to low-spin phase transition at around 2.62 a.u. Wigner-Seitz radius r_{WS} (equivalent to the lattice constant of 3.55 Å). At this point one can see a peculiarity in the shape of the EQOS of the FM fcc phase as well as a dramatic decrease of the magnetic moments on all atoms down to zero as r_{WS} decreases below this point (Figure 2 b).

3.1.2. Elastic constants of the fcc phase

Here, we would like to begin with the results on the elastic constants of the austenitic phase. Above 40 K, austenitic steels within the compositional range of Marval X12 have been found to be paramagnetic [63]. Therefore, in what follows, we are going to focus on the elastic properties of Marval X12 steel in the PM state.

We have employed EMTO-DLM DFT calculations of the PM fcc phase of $Fe_{76}Ni_{8.3}Cr_{12.6}Al_{1.4}Si_{0.1}Ti_{0.4}Mn_{0.03}Mo_{1.14}$ steel at both equilibrium theoretical and experimental [56] lattice parameters. We could not find any experimental data for comparison to our results on the elastic constants of the Marval X12 steel but we could compare the EMTO-DLM results to theoretical and experimental data on steels having close compositions to MarvalX12 steels (see Table 6) and found very reasonable agreement between all these data and our results. As we would expect based on our experience from previous investigations of iron and steel [32, 64, 65], 0K equilibrium DFT results underestimate the experimental lattice constant of $Fe_{76}Ni_{8.3}Cr_{12.6}Al_{1.4}Si_{0.1}Ti_{0.4}Mn_{0.03}Mo_{1.14}$ steel and respectively overestimate most of the elastic constants. However, calculations at experimental lattice constant provide generally better agreement between experimental and theoretical results [32, 64]. Relatively low values of C' (29 GPa) suggest a phonon mode softening in the system that is often associated with a possible phase transition (bcc/fcc) [66].

Based on the elastic constants of the fcc phase of Marval X12 steel calculated above, the elastic constants of the fcc phase of steels with increased carbon concentration are estimated. This estimation is based on the experimentally observed dependence of elastic constants on carbon concentration

Table 4: Elastic constants and elastic moduli (in GPa) of the fcc phase of $Fe_{76}Ni_{8.3}Cr_{12.6}Al_{1.4}Si_{0.1}Ti_{0.4}Mn_{0.03}Mo_{1.14}$ (MarvalX12-type) steel. Calculations have been done using the EMTO method at different lattice constants a_{lat} corresponding to experimental [56] (@exp) and theoretical equilibrium (@eq) values. The results have been compared to the results of Refs. [66–68]. Typical composition of Steel 316 shown for comparison normally includes 16-18% Cr 10-14% Ni.

		a_{lat} (Å)	Single cryst. El. Const.				Elastic modulus		
Source	Material	fcc, PM	C44	C11	C12	C'	B	G	E
		Current DFT results							
EMTO@eq	Marval	3.5433	158	225	128	49	160	98	245
EMTO@exp	Marval	3.5954	136	194	137	29	156	74	191
		Other DFT results							
Ref. [67]	$Fe_{70}Cr_{20}Ni_{10}$	3.6047	128	199	148	25	165	–	–
		Experimental data							
Ref. [66]	$Fe_{70}Cr_{15}Ni_{15}$	–	121	209	133	38	158	77	199
Ref. [66]	$Fe_{76}Cr_{12}Ni_{12}$	–	123	211	140	36	164	76	198
Ref. [68]	Steel316	–	119	206	133	37	157	–	–

of 304 stainless steels [69]. The elastic constants of fcc phase of different alloys used in the phase-field simulations are shown in Table-5.

3.1.3. Elastic constants of the bcc phase

We have calculated elastic properties of the FM $Fe_{76}Ni_{8.3}Cr_{12.6}Al_{1.4}Si_{0.1}Ti_{0.4}Mn_{0.03}Mo_{1.14}$ bcc alloy using the EMTO method. The calculations have been performed with two sets of lattice parameters including the theoretical equilibrium elastic constant at 0K and the experimental value for the ferrite in Marval X12 steel [56] (see Table 6). As in the case of the fcc phase (see the

Table 5: Alloy compositions and elastic constants (in GPa) of fcc phase used in phase-field simulations.

Alloy composition (at. %)	C_{11}	C_{12}	C_{44}
Fe-12.8Cr-8.5Ni	194	137	136
Fe-12.8Cr-8.5Ni-0.78C	192	136	135
Fe-12.8Cr-8.5Ni-1.8C	190	134	134
Fe-12.8Cr-8.5Ni-4.5C	185	132	134
Fe-12.8Cr-8.5Ni-5.75C	182	131	133

previous section), the DFT calculations at 0K predict lower lattice constants than experimental values and elastic constants calculations at theoretical lattice constants yield slightly higher values than those obtained at the experimental lattice constant. We could not find data on elastic constants of the bcc phase of the Marval X12 steel for comparison but our results are in good agreement with the theoretical data from Ref. [67] on a steel of a similar composition.

As the next step in our investigation, we have performed two sets of calculations using the exact composition of the Marval X12 steel and the one containing only the main alloying elements Cr and Ni: i) on $Fe_{76}Ni_{8.3}Cr_{12.6}Al_{1.4}$ $Si_{0.1}Ti_{0.4}Mn_{0.03}Mo_{1.14}$ and ii) on $Fe_{78.125}Ni_{9.375}Cr_{12.5}$ steels. The results have shown a small difference in the C_{ij} and elastic moduli for these two compositions. This result has allowed us to simplify the calculations of the multi-component Marval X12 steel to a three-component $Fe_{78.125}Ni_{9.375}Cr_{12.5}$ alloy that could also be modelled using the supercell (SC) approach (see Sec. 2.3) and the VASP-PAW method.

Results of the comparison between EMTO-CPA and VASP-PAW-SC cal-

culations demonstrate that both methods provide very close results on the equilibrium 0K lattice constants as well as on most of the elastic properties. The largest discrepancies are observed for C' (16 GPa), C_{11} (25 GPa), E (23 GPa) and G (10GPa). We refer to these differences as methodological assuming that VASP-PAW calculations may provide more accurate description of open structures than EMTO [45]. In addition, VASP-PAW calculations allow one to take into account the effect of local atomic relaxations (not included in EMTO-CPA calculations) that, however, appear to be very small (less than 4 GPa) for all elastic constants and moduli of $Fe_{78.125}Ni_{9.375}Cr_{12.5}$. However, the relaxation effects are very important for systems with C and, therefore, cannot be neglected [70]. In the following section, we will use the VASP-PAW calculations to investigate the effect of C on the elastic constants of the $Fe_{78.125}Ni_{9.375}Cr_{12.5}$ steel.

3.1.4. Elastic constants of the bct phase

Finally, we have investigated the effect of C on the lattice parameters and elastic properties of the bct martencitic phase of $Fe_{78.125}Ni_{9.375}Cr_{12.5}$ steel. In Figure 3, we show the results of VASP-PAW calculations of the steel with 0-6 at% of C. C has a crucial effect on the crystal structure of the bcc $Fe_{78.125}Ni_{9.375}Cr_{12.5}$ steel: C induces a tetragonal symmerty in the system with an increasing c/a ratio as C content increases as it is shown in Table 7. DFT calculations predict a more pronounced increase of the c/a ratio with increasing C-content in $Fe_{78.125}Ni_{9.375}Cr_{12.5}$ steel compared to pure Fe [29, 52] as it has been assumed in the c/a estimation based on the results from Ref. [29] shown in Table 3. This deviation, however, does not have a sizeable effect on the phase field results reported later. We have no experimental

Table 6: Elastic constants and elastic moduli (in GPa) of the bcc phase of $Fe_{76}Ni_{8.3}Cr_{12.6}Al_{1.4}Si_{0.1}Ti_{0.4}Mn_{0.03}Mo_{1.14}$ (MarvalX12-type) and $Fe_{78.125}Ni_{9.375}Cr_{12.5}$ steels. Calculations have been done using the EMTO and VASP methods at different lattice constants a_{lat} corresponding to experimental[56](@exp) and theoretical equilibrium (@eq) values. The results have been compared to the results of Ref. [67]. Vasp results are shown also for the case where atomic relaxations have been included in the calculation (rel).

		a_{lat} (Å)	Single cryst. El. Const.				Elastic modulus		
Source	Material	bcc, FM	C44	C11	C12	C'	B	G	E
		Current DFT results							
EMTO@eq	MarvalX12	2.8537	121	265	137	64	179	94	239
EMTO@exp	MarvalX12	2.8740	112	240	119	61	160	87	221
EMTO@eq	$Fe_{12}Cr_9Ni$	2.8486	117	261	136	62	178	91	233
VASP@eq	$Fe_{12}Cr_9Ni$	2.8546	117	236	144	46	175	81	210
VASP@eq(rel)	$Fe_{12}Cr_9Ni$	2.8548	117	236	140	48	172	82	211
		Other DFT results							
Ref. [67]	$Fe_{70}Cr_{20}Ni_{10}$	2.8432	126	273	142	65	186	–	–

data to compare with the DFT lattice constants of the bct phase. However, we presume that the absolute values of the lattice parameters from 0K DFT calculations underestimate the experimental values in a similar manner as observed in the cases of bcc and fcc phases. An underestimation of the experimental lattice constant [56] by 0.026 Åin the case of DFT calculations of the bcc phase is a typical deviation of the theoretical from the experimental values for Fe and its alloys [32, 64, 65, 71, 72]. This discrepancy is partly

related to the absence of the phonon contribution in the current DFT calculations and partly to the methodological aspects of the DFT description of Fe [64, 72].

The changes of of elastic constants and averaged polycrystalline moduli with C addition are shown in Figure 3 and Table 7, respectively. Our results suggest an increase of C_{11} and C_{33}, with no change in C_{13} and a slight decrease of C_{12}, C_{44} and C_{66} elastic constants. These results are consistent with available experimental data on the Fe-C system [73], where it has been shown that C_{11} and C_{33} increase; C_{13}, C_{12}, C_{44} and C_{66} decrease with increasing C content. A similar theoretical result has been obtained for the Fe-C system in Ref. [74] for most of the C_{ij} except for C_{11} and C_{33} which exhibited the opposite (to this work and to Ref. [73]) trend (decrease instead of an increase with increased C content).

Averaged bulk, Young's and shear moduli remain essentially unchanged in the whole range of considered C concentrations from 0 to 6 at.% (see Table 7). This is an interesting result suggesting a weak or no impact of C on the polycrystalline elastic moduli of the martensitic phase in $Fe_{78.125}Ni_{9.375}Cr_{12.5}$ and related MarvalX12-type of steels. Here, we assume that C will have the same effect on the elastic properties of the original Marval X12 steel (see Sec. 3.1.3 for details) and therefore the results for the C_{ij} of the bct phase of $Fe_{78.125}Ni_{9.375}Cr_{12.5}$ are used to model the martensitic transformation in Marval X12 steel using the phase-field simulations.

3.2. Phase-field simulations

The phase-field simulations predict that martensite morphology is lath-type in Marval X12 steel (Fig. 4), which is in good agreement with the

Table 7: Lattice constants and elastic moduli of the bcc phase of $Fe_{78.125}Ni_{9.375}Cr_{12.5}$-C steel. Lattice parameters have been obtained according to the procedure described in Sec. 2.3.

	Lattice constants			Elastic modulus (GPa)		
Conc., at. %	a, Å	b=c,Å	c/a	B	G	E
0	2.8548	2.8548	1.000	175	82	211
0.78	2.8498	2.8796	1.010	175	82	211
1.82	2.8370	2.9170	1.028	175	84	214
5.88	2.8049	3.0733	1.096	177	85	218

morphology observed in experiments by Tomimura et al [75] and in maraging steels that are similar in composition to the Marval X12 steel [76, 77]. The microstructure evolution (Fig. 4) shows that three variants of the martensite phase are formed. Variants 1,2 and 3 are shown in red, blue and green, respectively. Villa and Somers [78] have reported that lath martensite of type $\{557\}_{\gamma}$ is formed in Fe-12.8Cr-8.5Ni alloy. They reported that a martensite volume fraction of 79 % can be obtained on cooling to room temperature, whereas the present simulations predict that a martensite volume fraction of approximately 77 % can be obtained.

The microstructure evolution with an addition of 4.5 at. % carbon to Marval X12 steel is shown in Fig. 5. Although the simulation is started with variant-1, the local stress field causes it to completely shrink. The variants that can minimize the local stresses are favored. In this case variant-3 (green) is the most favorable one and hence grows to a larger extent compared to variants 1 (red) and 2 (blue). The microstructure is predominantly lath-type, although we observe formation of some plate-shaped units as shown in Figs. 6

and 7. Even a small amount of carbon (0.78 at. %) has a significant effect on microstructure as shown in Fig. 6b. We observe different martensite variants being dominant with increased carbon concentration of Marval X12 steel (Fig. 8a). Variant-1 is the dominant one in Marval X12 steel whereas variant-3 is the dominant one in the steel with 4.5 at. % carbon (Fig. 8a). The formation of different variant combinations leads to anisotropic mechanical properties, especially in steels subjected to ausforming [79].

In plain carbon steels, martensite morphology changes from lath to plate with increasing carbon concentration [15, 16]. The present simulations predict a mixed morphology, i.e. some variants in lath shape and some in plate shape. This is attributed to the presence of high concentrations of other alloying elements such as chromium and nickel. The increased tetragonality leads to variations in lattice constants as well as elastic constants. These variations affect the transformation strains and internal stresses, which lead to the formation of different variants.

The top view of the microstructure (Fig. 7a) shows that variants are formed in pairs in Marval X12 steel, similar to the microstructure observed in 301-type stainless steel [21]. The addition of carbon to Marval X12 steel does not lead to such a pairing, especially in the regions where plate-type units are formed (Fig. 7b and c). Figs. 4 - 8 show that variant-1 (red) is the most favored in Fe-12.8Cr-8.5Ni steel, whereas with an addition of carbon variant-3 (green) is the most favored variant.

The mean equivalent stress and plastic strain are estimated by calculating the local von Mises equivalent stress and plastic strain at each point in the simulation domain and then taking an average of all the respective values.

Fig. 8b shows that for a given volume fraction of martensite ($< 33\%$), the mean von Mises equivalent stress is large in Fe-12.8Cr-8.5Ni (Marval X12) steel and the stress levels decrease with increasing carbon content. The large stresses generated in Marval X12 steel are minimized through autocatalysis, i.e. formation of many new martensite variants that resemble laths. The autocatalytic nucleation of new martensite units causes a rapid increase in martensite volume fraction during this stage (Fig. 8a). Due to the formation of a sufficient number of martensite variants, stress decreases during the later stage of the transformation ($> 33\%$ volume fraction of martensite). Due to the relatively low stress levels in steels with higher carbon content, the degree of autocatalysis is relatively small compared to that in Marval X12 steel and hence some plate-type martensite units are observed in these steels.

Fig. 8c shows that for a given martensite volume fraction of upto 33 %, the mean equivalent plastic strain in Marval X12 steel is the lowest among all the alloys. In Marval X12 steel as the stresses are minimized through autocatalysis, plastic deformation is relatively small during this stage. Beyond this stage (> 33 % martensite volume fraction), the stresses are minimized through plastic deformation as the existing martensite units grow by shearing the austenite matrix and hence an increase in plastic strain is observed.

In high carbon steels, it has been reported that the transformation stresses are relieved through a combination of twinning in the midrib region of plate martensite and slip deformation in the regions adjacent to the midrib [80]. Therefore, the slip deformation in high carbon steels is not as large as that in low carbon steels. In the present model, the twinning in the midrib region of plate-shaped units is not included and hence the stress relaxation occurs

mainly through slip deformation. Therefore, during the initial stages of the transformation (< 33 % martensite volume fraction), we observe slightly larger plastic strain generated in the carbon-rich maraging steels compared to Marval X12 steel.

4. Conclusions

In this paper, we report the elastic properties of the fcc, bcc and bct phases of Marval X12 and Fe-[11.8-12.8]Cr-[5.9-9.3]Ni-[0-5.9]C steels obtained by means of DFT calculations. The results predict almost no changes of the polycrystalline bulk, Young's and shear moduli with an increase of C content and moderate monotonous changes of the single crystalline elastic constants of the martensitic phase. The main effect of C is related to the change of the crystal and elastic constants symmetry from cubic to tetragonal due to the martensitic phase transition.

The phase field simulations show that lath martensite is formed in Marval X12 steel, which is in good agreement with experimental observations. Addition of carbon above the typical values of Marval X12 steel gives rise to a mixed morphology containing lath and plate martensite. Presence of a higher carbon content leads to lower von Mises equivalent stress in the material and hence to a smaller degree of autocatalysis compared to that in Marval X12 steel. The relatively low stress levels in the steels with high carbon content gives rise to some coarse plate-type units compared to the finer lath-type units formed by autocatalysis in Marval X12 steel. During the initial stages of the transformation (< 33 % martensite volume fraction), the equivalent plastic strain in Marval X12 steel is the lowest among all the

alloys as autocatalysis is dominant during this stage. During the later stages, equivalent plastic strain in Marval X12 steel increases as the stresses are minimized through generation of plasticity by the growth of existing martensite units.

Data Availability

The raw data required to reproduce these findings are available to obtain from razvsevol@yahoo.com (DFT) and hemu23@gmail.com (phase field). The processed data required to reproduce these findings are available to obtain from razvsevol@yahoo.com (DFT) and hemu23@gmail.com (phase field)

Acknowledgements

The authors (V.R. and J.S.) gratefully acknowledge the financial support under the scope of the COMET program within the K2 Center Integrated Computational Material, Process and Product Engineering (IC-MPPE) (Project No 859480). This program is supported by the Austrian Federal Ministries for Transport, Innovation and Technology (BMVIT) and for Digital and Economic Affairs (BMDW), represented by the Austrian research funding association (FFG), and the federal states of Styria, Upper Austria and Tyrol. The ab initio computations performed within this work have been done at the Vienna Scientic Cluster (VSC). The phase-field simulations have been performed by using the HPC resources at Newcastle University, U.K. Dr. Frank Niessen is acknowledged for providing the thermodynamic driving forces using Thermo-Calc software. We would like to thank Prof. A. Ruban, Prof. T. Antretter and Dr. M. Petersmann for fruitful

discussions of the computational methodology used in this study and for providing experimental data on Marval X12 steel.

References

[1] Z. Huang, M. Abad, J. Ramsey, M. de Figueiredo, D. Kaoumi, N. Li, M. Asta, N. Gronbech-Jensen, P. Hosemann, A high temperature mechanical study on PH 13-8 Mo maraging steel, Mater. Sci. Eng. A 651 (2016) 574–582.

[2] S. Hossein Nedjad, J. Teimouri, A. Tahmasebifar, H. Shirazi, M. Nili Ahmadabadi, A new concept in further alloying of Fe-Ni-Mn maraging steels, Scripta Mater. 60 (2009) 528–531.

[3] E. Galindo-Nava, W. Rainforth, P. Rivera-Daz-del Castillo, Predicting microstructure and strength of maraging steels: Elemental optimisation, Acta Mater. 117 (2016) 270–285.

[4] S. Nedjad, M. Ahmadabad, T. Furuhara, Correlation between the inter granular brittleness and precipitation reactions during isothermal aging of and Fe-Ni-Mn maraging steel, Mater. Sci. Eng. A 490 (2008) 105–112.

[5] N. Heo, Ductile-brittle-ductile transition and grain boundary segregation of Mn and Ni in an Fe-6Mn-12Ni alloy, Scr. Mater. 34 (1996) 1517–1522.

[6] L. Shiang, M. Wayman, Maraging behavior of an Fe-19.SNi-5Mn alloy II: Evolution of reverse-transformed austenite during overaging , Metallography 21 (1988) 425–451.

[7] J. Pardal, S. Tavares, M. Cindra Fonseca, H. Abreu, J. Silva, Study of the austenite quantification by X-ray diffraction in the 18Ni-Co-Mo-Ti maraging 300 steel, J. Mater. Sci. 41 (2006) 2301–2307.

[8] H. Leitner, M. Schober, R. Schnitzer, S. Zinner, Strengthening behavior of Fe-Cr-Ni-Al-(Ti) maraging steels, Mater. Sci. eng. A 528 (2011) 5264–5270.

[9] S. Hossein Nedjad, A. Meimandi, S.and Mahmoudi, T. Abedi, S. Yazdani, H. Shirazi, M. Nili Ahmabadi, Effect of aging on the microstructure and tensile properties of Fe-Ni-Mn-Cr maraging alloys , Mater. Sci. eng. A 501 (2009) 182–187.

[10] K. Nagayama, Y. Kitajima, S. Kigami, K. Tanaka, F. Fischer, G. Cailletaud, Transformation induced plasticity in maraging steel: An experimental study , Key Eng. Mater. 177 (2000) 443–448.

[11] R. Schnitzer, G. Zickler, E. Lach, H. Clemens, S. Zinner, T. Lippmann, H. Leitner, Influence of reverted austenite on static and dynamic mechanical properties of a PH 13-8 Mo maraging steel , Mater. Sci. Eng. A 527 (2010) 2065–2070.

[12] J. Talonen, Effect of strain-induced alpha-martensite transformation on mechanical properties of metastable austenitic stainless steels, PhD thesis, Helsinki University of Technology, Helsinki, 2007.

[13] M. El-Fawkhry, M. Eissa, A. Fathy, T. Mattar, Development of maraging steel with retained austenite in martensite matrix, Mater. Today: Proc. 2S (2015) S711 – S714.

[14] A. Beltyukov, V. Stepanov, A. Shein, Effect of carbon on the properties of corrosion-resistant maraging steels without titanium, Metallov. 11 (1989) 24–26.

[15] G. Krauss, A. Marder, The morphology of martensite in iron alloys, Metall. Trans. 2 (1971) 2343–2357.

[16] P. Kelly, J. Nutting, The martensite transformation in carbon steels, Proc. Roy. Soc. 259 (1960) 45–48.

[17] N. Moelans, B. Blanpain, P. Wollants, An introduction to phase-field modeling of microstructure evolution, CALPHAD 32 (2008) 268–294.

[18] L. Chen, Phase-field models for microstructure evolution, Annu. Rev. Mater. Res. 32 (2002) 113–140.

[19] H. K. Yeddu, A. Malik, J. Å gren, G. Amberg, A. Borgenstam, Three-dimensional phase-field modeling of martensitic microstructure evolution in steels, Acta Mater. 60 (2012) 1538–1547.

[20] A. Artemev, Y. Jin, A. Khachaturyan, Three-dimensional phase field model of proper martensitic transformation, Acta Mater. 49 (2001) 1165–1177.

[21] H. K. Yeddu, A. Borgenstam, J. Å gren, Effect of martensite embryo potency on the martensitic transformations in steels - A 3D phase-field study, J. Alloys. Compd. 577S (2013) S141–S146.

[22] A. Yamanaka, T. Takaki, Y. Tomita, Elastoplastic phasefield simula-

tion of self- and plastic accommodations in cubic tetragonal martensitic transformation, Mater. Sci. Eng. A 491 (2008) 378–384.

[23] H. K. Yeddu, V. I. Razumovskiy, A. Borgenstam, P. A. Korzhavyi, A. V. Ruban, J. gren, Multi-length scale modeling of martensitic transformations in stainless steels, Acta Materialia 60 (19) (2012) 6508 – 6517.

[24] T. W. Heo, L. Q. Chen, Phase-field modeling of displacive phase transformations in elastically anisotropic and inhomogeneous polycrystals, Acta Mater. 76 (2014) 68–81.

[25] H. K. Yeddu, Phase-field modeling of austenite grain size effect on martensitic transformation in stainless steels, Comp. Mater. Sci. 154 (2018) 75–83.

[26] M. Javanbakht, V. Levitas, Interaction between phase transformations and dislocations at the nanoscale Part 2 Phase field simulation examples, J. Mech. Phys. Solids 82 (2015) 164–185.

[27] H. K. Yeddu, T. Lookman, A. Saxena, Reverse phase transformation of martensite to austenite in stainless steels: a 3D phase-field study, J. Mater. Sci. 49 (2014) 3642–3651.

[28] H. K. Yeddu, T. Lookman, A. Saxena, Strain-induced martensitic transformation in stainless steels: A three-dimensional phase-field study, Acta Mater. 61 (2013) 6972–6982.

[29] Z. Nishiyama, Martensitic Transformation, Academic Press, New York, USA., 1978.

[30] J. Andersson, L. Helander, T. andHöglund, P. Shi, B. Sundman, THERMO-CALC & DICTRA computational tools for materials science, CALPHAD 26 (2002) 273–312.

[31] M. J. Mehl, B. M. Klein, D. A. Papaconstantopoulos, First principles calculations of elastic properties of metals, in: J. H. Westbrook, R. L. Fleischer (Eds.), In- termetallic Compounds: Principles and Practice, Vol. 1, John Wiley & Sons, London, 1995, pp. 195–210.

[32] V. I. Razumovskiy, A. V. Ruban, P. A. Korzhavyi, First-principles study of elastic properties of cr- and fe-rich fe-cr alloys, Phys. Rev. B 84 (2011) 024106. doi:10.1103/PhysRevB.84.024106.
URL https://link.aps.org/doi/10.1103/PhysRevB.84.024106

[33] W. Voigt, Ueber die beziehung zwischen den beiden elasticittsconstanten isotroper krper, Annalen der Physik 274 (12) 573–587. arXiv:https://onlinelibrary.wiley.com/doi/pdf/10.1002/andp.18892741206, doi:10.1002/andp.18892741206.
URL https://onlinelibrary.wiley.com/doi/abs/10.1002/andp.18892741206

[34] A. Reuss, Berechnung der fliegrenze von mischkristallen auf grund der plastizittsbedingung fr einkristalle ., ZAMM - Journal of Applied Mathematics and Mechanics / Zeitschrift fr Angewandte Mathematik und Mechanik 9 (1) 49–58. arXiv:https://onlinelibrary.wiley.com/doi/pdf/10.1002/zamm.19290090104, doi:10.1002/zamm.19290090104.
URL https://onlinelibrary.wiley.com/doi/abs/10.1002/zamm.19290090104

[35] R. Hill, The elastic behaviour of a crystalline aggregate, Proceedings of the Physical Society. Section A 65 (5) (1952) 349.
URL http://stacks.iop.org/0370-1298/65/i=5/a=307

[36] P. E. Blöchl, Projector augmented-wave method, Phys. Rev. B 50 (1994) 17953–17979. doi:10.1103/PhysRevB.50.17953.
URL http://link.aps.org/doi/10.1103/PhysRevB.50.17953

[37] G. Kresse, D. Joubert, From ultrasoft pseudopotentials to the projector augmented-wave method, Phys. Rev. B 59 (1999) 1758.

[38] G. Kresse, J. Furthmller, Efficiency of ab-initio total energy calculations for metals and semiconductors using a plane-wave basis set, Comput. Mat. Sci. 6 (1996) 15.

[39] G. Kresse, J. Furthmller, Efficient iterative schemes for ab initio total-energy calculations using a plane-wave basis set, Phys. Rev. B 54 (1996) 11169.

[40] J. P. Perdew, K. Burke, M. Ernzerhof, Generalized gradient approximation made simple, Phys. Rev. Lett. 77 (1996) 3865–3868. doi:10.1103/PhysRevLett.77.3865.
URL https://link.aps.org/doi/10.1103/PhysRevLett.77.3865

[41] J. P. Perdew, K. Burke, M. Ernzerhof, Generalized gradient approximation made simple [phys. rev. lett. 77, 3865 (1996)], Phys. Rev. Lett. 78 (1997) 1396–1396. doi:10.1103/PhysRevLett.78.1396.
URL https://link.aps.org/doi/10.1103/PhysRevLett.78.1396

[42] H. J. Monkhorst, J. D. Pack, Special points for brillouin-zone integrations, Physical Review B 13 (12) (1976) 5188–5192.

[43] O. K. Andersen, O. Jepsen, G. Krier, Methods of Electronic Structure Calculations, World Scientific, 1994.

[44] R. Tank, C. Arcangeli, An introduction to the third-generation lmto method, physica status solidi (b) 217 (1) (2000) 89–130. doi:10.1002/(SICI)1521-3951(200001)217:1¡89::AID-PSSB89¿3.0.CO;2-C.
URL http://dx.doi.org/10.1002/(SICI)1521-3951(200001)217:1<89::AID-PSSB89>3.0

[45] L. Vitos, Computational Quantum Mechanics for Materials Engineers: The EMTO Method and Applications, Engineering Materials and Processes, Springer, 2007.
URL http://books.google.at/books?id=4pqDtgAACAAJ

[46] B. L. Gyorffy, Coherent-potential approximation for a nonoverlapping-muffin-tin-potential model of random substitutional alloys, Phys. Rev. B 5 (1972) 2382–2384. doi:10.1103/PhysRevB.5.2382.
URL https://link.aps.org/doi/10.1103/PhysRevB.5.2382

[47] M. Cyrot, Phase transition in hubbard model, Phys. Rev. Lett. 25 (1970) 871–874. doi:10.1103/PhysRevLett.25.871.
URL http://link.aps.org/doi/10.1103/PhysRevLett.25.871

[48] B. L. Gyorffy, A. J. Pindor, J. Staunton, G. M. Stocks, H. Winter, A first-principles theory of ferromagnetic phase transitions in metals,

Journal of Physics F: Metal Physics 15 (6) (1985) 1337.
URL http://stacks.iop.org/0305-4608/15/i=6/a=018

[49] O. E. Peil, A. V. Ruban, B. Johansson, Self-consistent supercell approach to alloys with local environment effects, Phys. Rev. B 85 (2012) 165140. doi:10.1103/PhysRevB.85.165140.
URL http://link.aps.org/doi/10.1103/PhysRevB.85.165140

[50] F. Birch, Finite elastic strain of cubic crystals, Phys. Rev. 71 (1947) 809–824. doi:10.1103/PhysRev.71.809.
URL https://link.aps.org/doi/10.1103/PhysRev.71.809

[51] K. Momma, F. Izumi, *VESTA3* for three-dimensional visualization of crystal, volumetric and morphology data, Journal of Applied Crystallography 44 (6) (2011) 1272–1276. doi:10.1107/S0021889811038970.
URL http://dx.doi.org/10.1107/S0021889811038970

[52] O. D. Sherby, J. Wadsworth, D. Lesuer, C. Syn, The c/a Ratio in Quenched Fe-C and Fe-N Steels - A Heuristic Story, Materials Science Forum 539-543 (2007) 215–222. doi:10.4028/www.scientific.net/MSF.539-543.215.
URL http://www.scientific.net/MSF.539-543.215

[53] Z. Guo, C. Lee, J. Morris Jr., On coherent transformations in steel, Acta Mater. 52 (2004) 5511–5518.

[54] H. K. Yeddu, Martensitic transformations in steels - A 3D phase-field study, PhD thesis, KTH Royal Institute of Technology, Sweden, 2012.

[55] E. De souza Neto, D. Peric, D. Owen, Computational methods for plasticity - Theory and applications, John Wiley and Sons Ltd., West Sussex (UK), 2008.

[56] X-Ray measurements. Courtesy of Prof. Thomas Antretter, Montanuniversitaẗ Leoben, Austria.

[57] T. Antretter, F. Fischer, T. Lube, K. Tanaka, G. Cailletaud, The Thermo-mechanical Response to a General Loading Path of a Martensitically Transforming Steel, J. Intell. Mater. Sys. Struct. 13 (2002) 811–815.

[58] W. D. Callister Jr., Fundamentals of materials science and engineering, John Wiley, New York, USA., 2001.

[59] G. Krauss, Martensite in steel: strength and structure, Mater. Sci. Eng. A 273-275 (1999) 40–57.

[60] C. Moosbrugger, Atlas of stress–strain curves, 2nd ed. , ASM International, Materials Park, OH, USA., 2002.

[61] G. Amberg, R. Tönhardt, C. Winkler, Finite element simulations using symbolic computing, Math. and Comp. in Sim. 49 (1999) 257–274.

[62] K. Nagayama, T. Terasaki, K. Tanaka, F. Fischer, T. Antretter, G. Cailletaud, F. Azzouz, Mechanical properties of a Cr-Ni-Mo-Al-Ti maraging steel in the process of martensitic transformation, Mater. Sci. Eng. A 308 (2001) 25–37.

[63] A. K. Majumdar, P. v. Blanckenhagen, Magnetic phase diagram of $fe_{80-x}ni_xcr_{20}$ ($10 \leq x \leq 30$) alloys, Phys. Rev. B 29 (1984) 4079–4085. doi:10.1103/PhysRevB.29.4079.
URL https://link.aps.org/doi/10.1103/PhysRevB.29.4079

[64] V. I. Razumovskiy, A. V. Ruban, P. A. Korzhavyi, Effect of temperature on the elastic anisotropy of pure fe and $fe_{0.9}cr_{0.1}$ random alloy, Phys. Rev. Lett. 107 (2011) 205504. doi:10.1103/PhysRevLett.107.205504.
URL https://link.aps.org/doi/10.1103/PhysRevLett.107.205504

[65] V. I. Razumovskiy, A. Reyes-Huamantinco, P. Puschnig, A. V. Ruban, Effect of thermal lattice expansion on the stacking fault energies of fcc fe and $fe_{75}mn_{25}$ alloy, Phys. Rev. B 93 (2016) 054111. doi:10.1103/PhysRevB.93.054111.
URL https://link.aps.org/doi/10.1103/PhysRevB.93.054111

[66] A. Teklu, H. Ledbetter, S. Kim, L. A. Boatner, M. McGuire, V. Keppens, Single-Crystal Elastic Constants of Fe-15Ni-15Cr Alloy, Metallurgical and Materials Transactions A 35A (October) (2004) 3149–3154.

[67] H. Zhang, B. Johansson, R. Ahuja, L. Vitos, First-principles study of solid-solution hardening in steel alloys, Computational Materials Science 55 (2012) 269–272. doi:10.1016/j.commatsci.2011.12.020.
URL http://linkinghub.elsevier.com/retrieve/pii/S0927025611006811

[68] R. P. Reed, T. Horiuchi, Austenitic Steels at Low Temperatures, Plenum press, New York and London, 1983. doi:10.1007/978-1-4613-

3730-0.
URL http://link.springer.com/10.1007/978-1-4613-3730-0%5Cnhttp://link.springe

[69] H. Ledbetter, M. Austin, Effects of carbon and nitrogen on the elastic constants of AISI type 304 stainless steel, Mater. Sci. Eng. 70 (1985) 143–149.

[70] D. E. Jiang, E. A. Carter, Carbon dissolution and diffusion in ferrite and austenite from first principles, Phys. Rev. B 67 (2003) 214103. doi:10.1103/PhysRevB.67.214103.
URL https://link.aps.org/doi/10.1103/PhysRevB.67.214103

[71] P. Haas, F. Tran, P. Blaha, Calculation of the lattice constant of solids with semilocal functionals, Phys. Rev. B 79 (2009) 085104. doi:10.1103/PhysRevB.79.085104.
URL https://link.aps.org/doi/10.1103/PhysRevB.79.085104

[72] A. V. Ruban, V. I. Razumovskiy, First-principles based thermodynamic model of phase equilibria in bcc fe-cr alloys, Phys. Rev. B 86 (2012) 174111. doi:10.1103/PhysRevB.86.174111.
URL https://link.aps.org/doi/10.1103/PhysRevB.86.174111

[73] S. A. Kim, W. L. Johnson, Elastic constants and internal friction of martensitic steel, ferritic-pearlitic steel, and α-iron, Materials Science and Engineering A 452-453 (2007) 633–639. doi:10.1016/j.msea.2006.11.147.

[74] M. Souissi, H. Numakura, Elastic Properties of FeC and FeN Martensites, ISIJ International 55 (7) (2015) 1512–1521.

doi:10.2355/isijinternational.55.1512.
URL https://www.jstage.jst.go.jp/article/isijinternational/55/7/55_1512/_artic

[75] K. Tomimura, H. Nagamori, S. Takaki, Y. Tokunaga, Tensile deformation behavior in metastable austenitic stainless steel having ultra fine-grain structure, J. Japan Inst. of Met. 55 (1991) 376–382.

[76] Y. Lian, J. Huang, J. Zhang, C. Zhao, W. Gao, Z. Zhang, M. Ma, Effects of cold rolling on the microstructure and properties of Fe-Cr-Ni-MoTi maraging steel, Mater. Sci. Eng. A 712 (2018) 663–670.

[77] T. Simm, L. Sun, D. Galvin, M. Hill, P. andRawson, S. Birosca, E. P. Gilbert, H. Bhadeshia, K. Perkins, The Effect of a Two-Stage Heat-Treatment on the Microstructural and Mechanical Properties of a Maraging Steel, Materials 10 (2017) 1346.

[78] M. Villa, M. Somers, Thermally activated martensite formation in ferrous alloys, Scr. Mater. 142 (2018) 46–49.

[79] G. Miyamoto, N. Iwata, N. Takayama, T. Furuhara, Variant selection of lath martensite and bainite transformation in low carbon steel by ausforming, J. Alloys. Compd. 577 (2013) S528–S532.

[80] A. Stormvinter, P. Hedström, A. Borgenstam, A Transmission electron microscopy study of plate martensite formation in high-carbon low alloy steels, J. Mater. Sci. Tech. 29 (2013) 373–379.

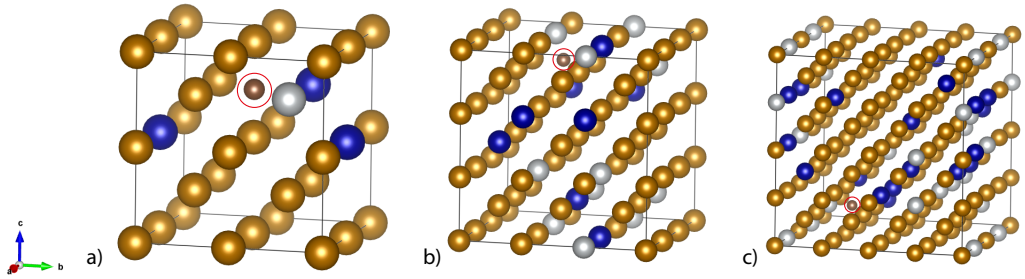

Figure 1: Supercells used to model Fe-Cr-Ni disordered alloys with C: a) $Fe_{76.48}Cr_{11.76}Ni_{5.88}C_{5.88}$), a 17-atom SC; b) $Fe_{76.36}Cr_{12.72}Ni_{9.10}C_{1.82}$, a 55-atom SC; c) $Fe_{77.52}Cr_{12.40}Ni_{9.30}C_{0.78}$, a 129-atom SC. Brown spheres represent Fe, blue represent Cr, light grey represent Ni and dark brown marked by a red circle around them represent C atoms respectively.

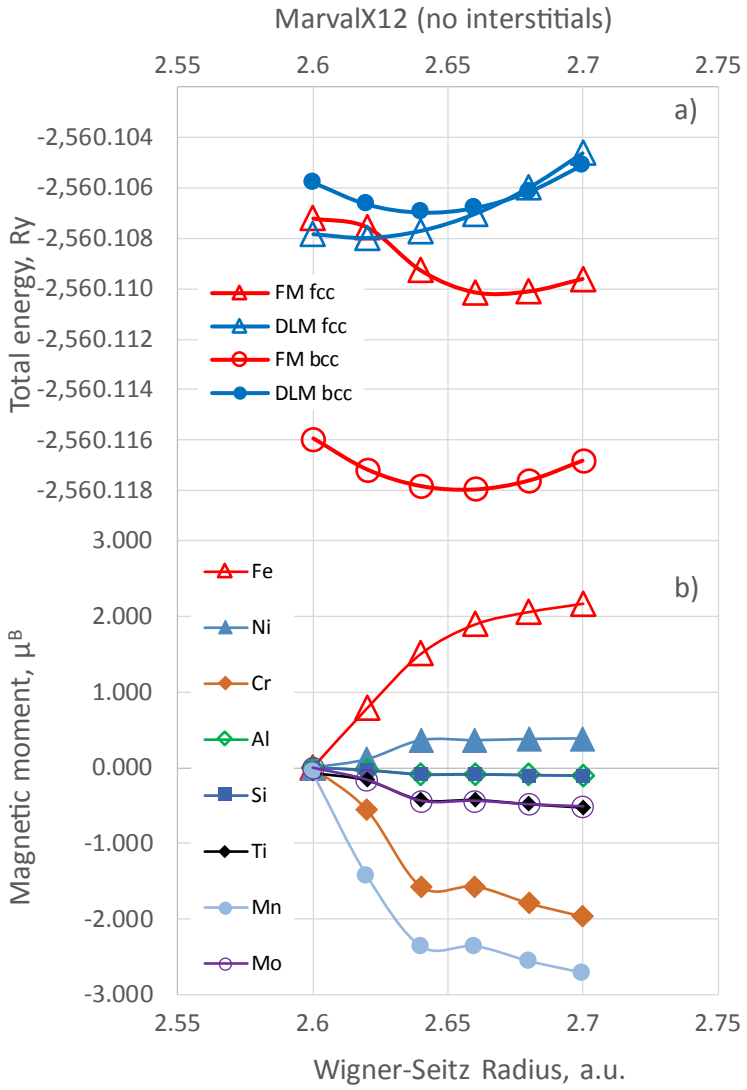

Figure 2: a) Equation of state (EQOS) for bcc and fcc phases of $Fe_{76}Ni_{8.3}Cr_{12.6}Al_{1.4}Si_{0.1}Ti_{0.4}Mn_{0.03}Mo_{1.14}$ (MarvalX12-type steel) [62]. The picture shows the EQOS for two different magnetic states: the ferromagnetic (FM) and the paramagnetic state realized via the disordered local moment (DLM) model calculations. b) Magnetic moments on atoms in the FM fcc phase.

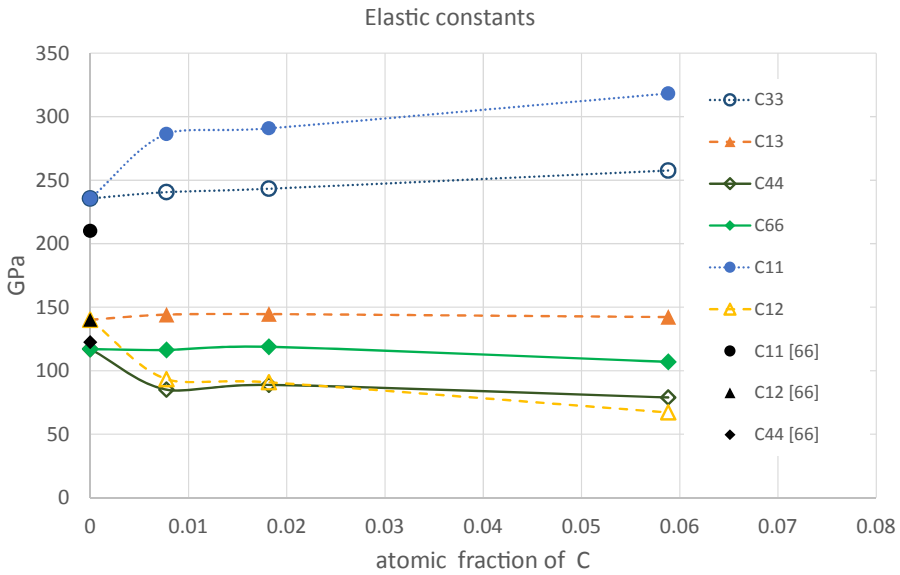

Figure 3: Elastic constants of $Fe_{78.125}Ni_{9.375}Cr_{12.5}$-C steel as a function of C-content. DFT results for bcc $Fe_{78.125}Ni_{9.375}Cr_{12.5}$ are compared to room-temperature elastic constants measurements of fcc $Fe_{76}Ni_{12}Cr_{12}$ from Ref. [66].

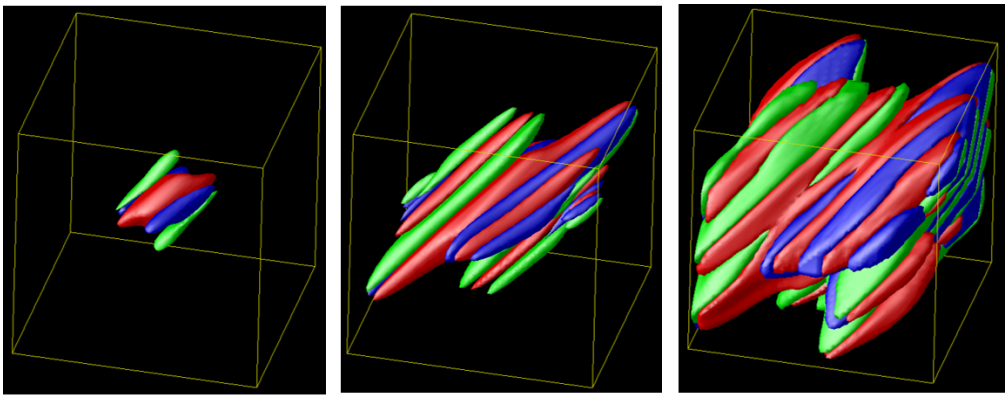

Figure 4: Lath martensite formation in Fe-12.8Cr-8.5Ni steel at (a) t*= 5 (b) t*= 10 and (c) t*= 100.

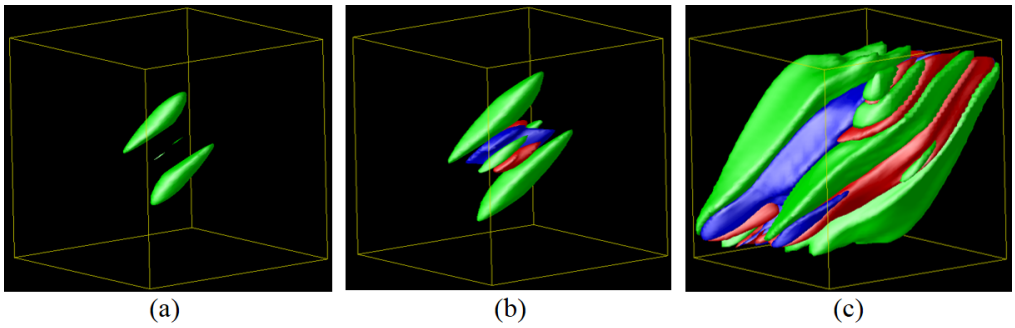

Figure 5: Martensite formation in Fe-12.8Cr-8.5Ni-4.5C steel at (a) t*= 15 (b) t*= 20 and (c) t*= 100.

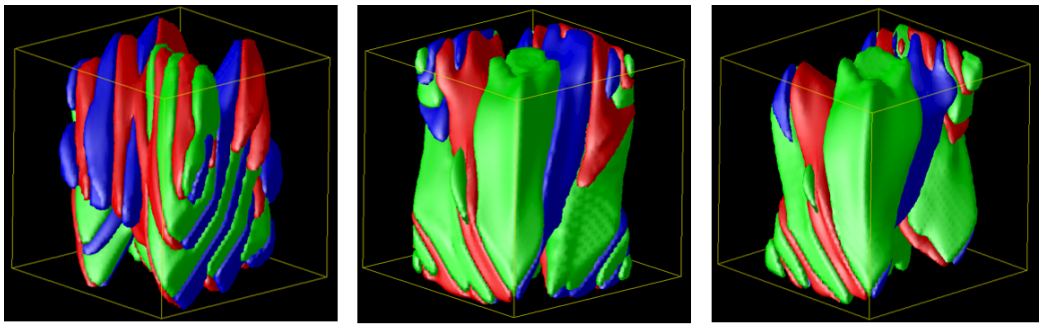

Figure 6: Microstructures obtained at t*=100 in (a) Fe-12.8Cr-8.5Ni (b) Fe-12.8Cr-8.5Ni-0.78C and (c) Fe-12.8Cr-8.5Ni-4.5C steels.

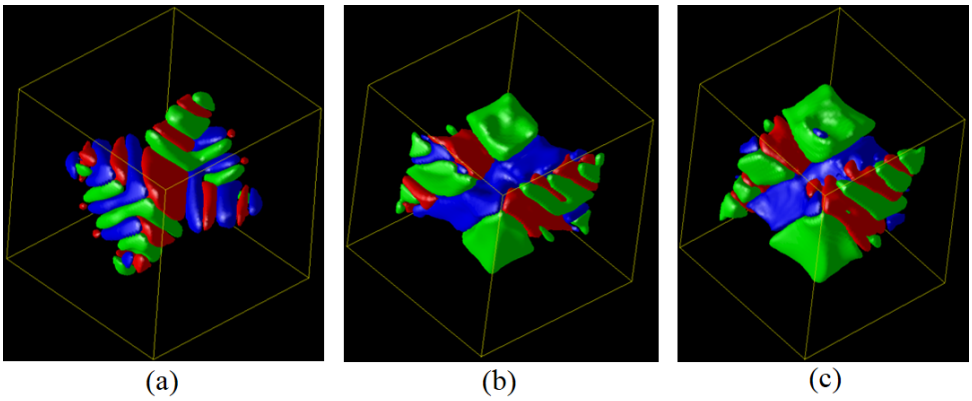

Figure 7: Top view of microstructures in (a) Fe-12.8Cr-8.5Ni steel at t*=25 (b) Fe-12.8Cr-8.5Ni-1.8C steel at t*=100 and (c) Fe-12.8Cr-8.5Ni-5.75C steel at t*=100.

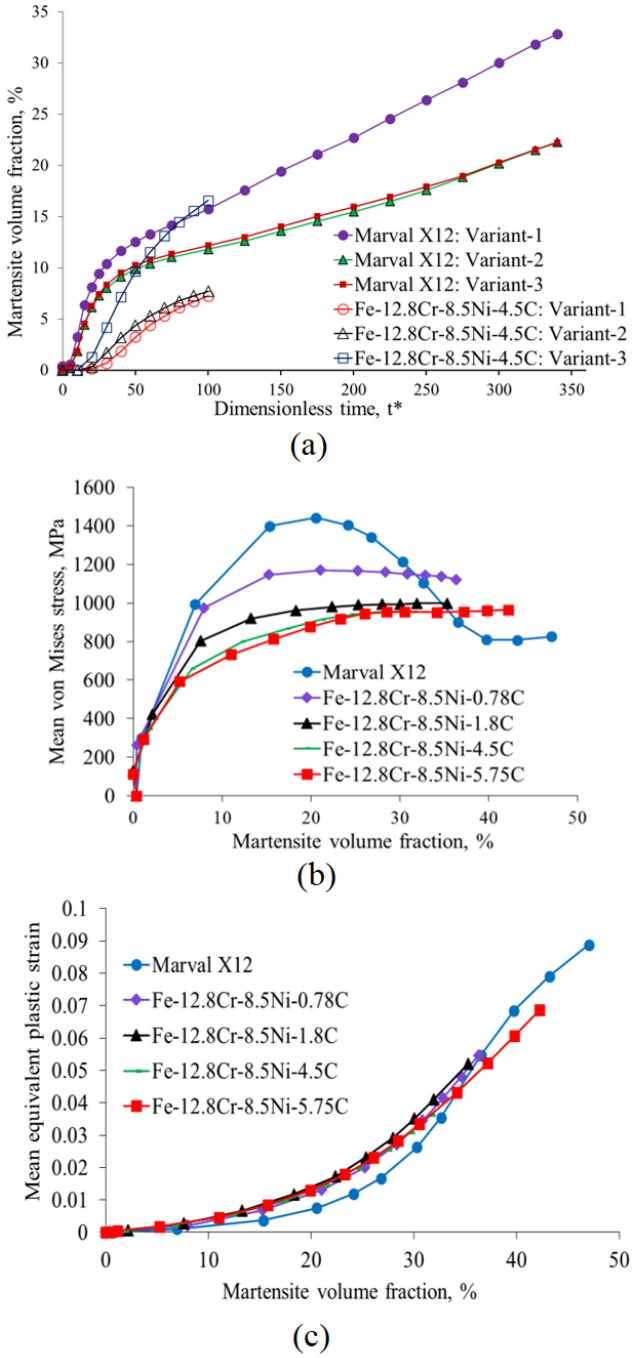

Figure 8: Variation of (a) volume fraction with t* (b) mean von Mises equivalent stress and (c) mean equivalent plastic strain with martensite volume fraction in different alloys.